Continuous, multidimensional coding of 3D complex tactile stimuli by primary sensory neurons of the vibrissal system

Nicholas E. Bush[a], Sara A. Solla[b,c], and Mitra J. Z. Hartmann[d,e,1]

[a]Interdepartmental Neuroscience Program, Northwestern University, Evanston, IL 60208; [b]Department of Physics and Astronomy, Northwestern University, Evanston, IL 60208; [c]Department of Physiology, Northwestern University, Chicago, IL 60611; [d]Department of Biomedical Engineering, Northwestern University, Evanston, IL 60208; and [e]Department of Mechanical Engineering, Northwestern University, Evanston, IL 60208

Edited by Peter L. Strick, University of Pittsburgh, Pittsburgh, PA, and approved May 21, 2021 (received for review December 3, 2020)

Across all sensory modalities, first-stage sensory neurons are an information bottleneck: they must convey all information available for an animal to perceive and act in its environment. Our understanding of coding properties of primary sensory neurons in the auditory and visual systems has been aided by the use of increasingly complex, naturalistic stimulus sets. By comparison, encoding properties of primary somatosensory afferents are poorly understood. Here, we use the rodent whisker system to examine how tactile information is represented in primary sensory neurons of the trigeminal ganglion (Vg). Vg neurons have long been thought to segregate into functional classes associated with separate streams of information processing. However, this view is based on Vg responses to restricted stimulus sets which potentially underreport the coding capabilities of these neurons. In contrast, the current study records Vg responses to complex three-dimensional (3D) stimulation while quantifying the complete 3D whisker shape and mechanics, thereby beginning to reveal their full representational capabilities. The results show that individual Vg neurons simultaneously represent multiple mechanical features of a stimulus, do not preferentially encode principal components of the stimuli, and represent continuous and tiled variations of all available mechanical information. These results directly contrast with proposed codes in which subpopulations of Vg neurons encode select stimulus features. Instead, individual Vg neurons likely overcome the information bottleneck by encoding large regions of a complex sensory space. This proposed tiled and multidimensional representation at the Vg directly constrains the computations performed by more central neurons of the vibrissotrigeminal pathway.

sensory | trigeminal | whisker | vibrissa | encoding

Sensory neuroscience aims to quantify how neurons encode and process fundamental physical stimuli: photons, pressure waves, chemicals, and mechanical forces. A common experimental approach is to use controlled, reduced, and repeatable stimulus sets to elicit consistent neural responses that can be averaged to reduce trial-to-trial variability (1–6). This method lends itself to a description of neural coding in which neurons are tuned to a small number of stimulus features (7) and to a categorization of neurons into functional classes (8) based on their differential responses to those preselected features of the stimuli (1, 3, 5, 9–12). A problem with this approach is that results are constrained by stimuli that are typically categorical and significantly underrepresent the stimulus space to which the neurons respond. It is thus almost inevitable that the neurons will, in turn, exhibit simple, low-dimensional tuning curves and categorical response types. Descriptions of neural representations of stimuli therefore remain incomplete.

The rodent whisker system is one of the premier models for studying tactile processing and cortical function (13). During natural exploration, rodents move their whiskers in rhythmic, nonrepeatable three-dimensional (3D) trajectories (14, 15) generating complex, continuously varying patterns of tactile input. However, most descriptions of vibrissal-responsive primary sensory neurons in the trigeminal ganglion (Vg) are based on experiments that use reduced stimulus sets in which variations in the presented stimuli are discrete, involving only a few features or limited spatial directions, small in dynamic range, or presented only along the neuron's preferred direction. Recent work in awake, whisking animals has employed a more continuous stimulus set, but these studies have been restricted to a two-dimensional (2D) analysis of whisker motion (16–19).

Here, we take inspiration from studies of the visual system that employ increasingly complex stimulus sets (20, 21) and apply to the whiskers a manual, naturalistically varying stimulus set designed for a rich exploration of the tactile stimulus space. The stimuli employed here span ranges similar to those observed in naturally behaving animals (22, 23) (*SI Appendix*, Fig. S2). We introduce a stereo-vision 3D whisker imaging technique, apply a model of 3D whisker mechanics (24), and implement recently developed statistical modeling techniques (25, 26) to characterize the 3D input space available to the whisker system and the consequent response properties of Vg neurons.

When characterized through the expanded naturalistic stimulus set employed here, the response properties of Vg neurons reveal a fundamentally different encoding structure than generally appreciated. We find that Vg neurons are broadly tuned across multiple stimulus features, including force, bending moment, and rotation, as well as stimulation direction. These neurons do not represent select mechanical features, nor do they

Significance

An animal's primary sensory neurons (PSNs) translate information about the environment into neural signals that allow perception and action. While much is known about visual and auditory PSN responses to complex stimuli, somatosensory neurons have been characterized with simplified and repeatable stimuli. Thus, knowledge of somatosensory PSN representational capacity remains incomplete. We used the rodent whisker system to examine how tactile mechanical information is represented in PSNs of the trigeminal ganglion (Vg) when the whiskers receive complex three-dimensional stimulation. In contrast to proposed codes in which subpopulations of Vg neurons encode select stimulus features, our results show that individual Vg neurons represent multiple stimulus features in a tiled and continuous manner, thus encoding large regions of a complex sensory space.

Author contributions: N.E.B. and M.J.Z.H. designed research; N.E.B. performed research; N.E.B., S.A.S., and M.J.Z.H. analyzed data; and N.E.B., S.A.S., and M.J.Z.H. wrote the paper.

The authors declare no competing interest.

This article is a PNAS Direct Submission.

[1]To whom correspondence may be addressed. Email: hartmann@northwestern.edu.

This article contains supporting information online at https://www.pnas.org/lookup/suppl/doi:10.1073/pnas.2020194118/-/DCSupplemental.

Published August 5, 2021.

represent the structure of the leading principal components that span a low-dimensional subspace of the mechanical stimuli space. Importantly, these diffuse representations of mechanical stimuli continuously tile the stimulus space used here, suggesting that primary sensory neurons possibly use a dense or near dense coding scheme to represent tactile stimuli. Thus, Vg neurons do not segregate into functional classes that convey specialized feature information to more central structures (4, 27, 28).

An important lesson conveyed by these results is the crucial fact that descriptions of the response properties of sensory neurons are fundamentally constrained by the complexity and extent of the stimulus sets used to probe them, and that stimulus sets that underrepresent the complexity and extent of natural stimuli can lead to incomplete, if not incorrect, descriptions of the encoding properties of these neurons. The stimuli used in the present experiments are not exhaustive of all possible stimuli explored during natural, active exploration; in particular, we do not probe the realm of fine-scale temporal dynamics that arise during interactions with textured objects. Even within these limitations, the results presented here indicate that individual Vg neurons represent complex features of 3D deformations that have been untested until now.

Results

Acquisition of 3D Stimulus Information. We recorded 78 whisker-responsive Vg neurons in 22 anesthetized rats during manual tactile stimulation of single whiskers. During stimulation, high-speed video (300 or 500 fps) captured whisker motion in two views (Fig. 1*A*). Following previous methods (29), a handheld graphite probe was used to repeatedly deflect the whisker at two to three different distances along its length (Fig. 1*C*) in eight cardinal directions (Fig. 1*D*). Because of the variable nature of the manual stimulation, we do not characterize deflections by the specific value of arclength of probe contact or the direction of deflection. Instead, we classify each deflection into an arclength group and direction group via unsupervised clustering methods (*SI Appendix*, *Extended Methods*: Identification of direction and arclength groups). In addition, both stimulation speed and the subsequent contact duration varied across trials. We attempted to deflect the whisker at two discrete speeds, but intrinsic stimulation variability resulted in a unimodal distribution of stimulation speeds (median probe speed = 19.6 mm/s, interquartile range [IQR] = [11, 34] mm/s; median contact duration = 147 ms, IQR = [95, 251] ms). Distributions of stimulus parameters calculated post hoc from video data across all experiments and contacts are shown in *SI Appendix*, Fig. S2.

Video and neural data were recorded for an average of ∼500 s per neuron, with an average of 684 whisker deflections across all conditions per whisker. Whiskers were tracked in both camera views (30); the 3D whisker shape and stimulus contact point were reconstructed (Fig. 1*B*) by registering the tracked whisker into a common 3D reference frame (*SI Appendix*, *Extended Methods*: 3D whisker reconstruction). The code to register 3D whiskers is hosted at https://github.com/SeNSE-lab/VG3D-merge. Mechanical models (24) were used to compute forces and moments at the whisker base for each video frame (Fig. 1*E*).

In the anesthetized animal, exerting a force on a whisker causes the whisker to bend and the follicle to rotate within the mystacial pad (29). This rotation generates a force between the follicle and surrounding tissue that may contribute to Vg responses. Because the mechanical properties of the follicle–cheek interface are unknown, we used the whisker's angular rotation as it emerged from the cheek (Fig. 1*E* and *SI Appendix*, Fig. S1) as a proxy for the force of the tissue on the follicle. All signals, including spike times, were interpolated and binned at 1 kHz.

The variability inherent in manual deflections precludes comparing time-locked responses across trials. However, each manual deflection evolved similarly over time as would occur during repeated whisks against an object. This temporal structure lends itself to "time-normalized" analyses in which stimulation durations are normalized to one (16, 28).

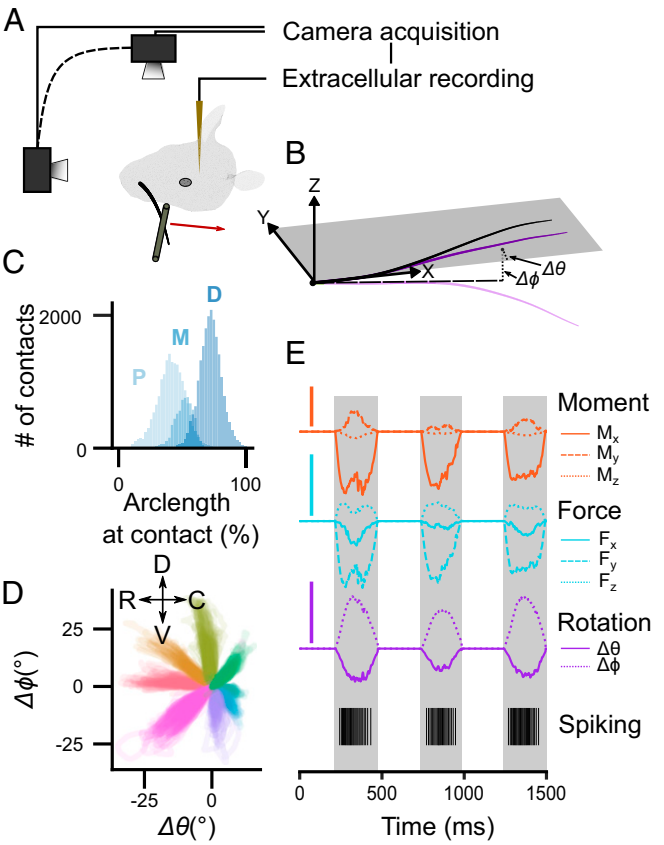

Fig. 1. Acquisition of 3D stimulus information. (*A*) Schematic of experimental setup. A tungsten electrode records activity from a Vg neuron as manual deflections of a single whisker are monitored with two high-speed cameras. (*B*) Example 3D reconstruction of a whisker. Mechanics are calculated in whisker-centered coordinates based on whisker shape changes (bending; light purple). Rotational features are calculated based on changes in base segment emergence angles (light purple, $\Delta\theta$ in the *x-y* plane, $\Delta\phi$ in the *x-z* plane) compared to rest (black whisker). (*C*) Deflections were applied at two or three distances along the whisker arclength; whisker arclengths were normalized to one and contacts sorted into three "distance groups": proximal (P), middle (M), and distal (D). A histogram of the number of contacts at a given arclength is shown across all neurons. When only two distinct clusters were found for a given whisker, the middle group was omitted and is thus underrepresented. (*D*) Deflections were applied in approximately eight directions in the plane perpendicular to the whisker's primary axis and sorted into eight "direction groups." Trajectories described in terms of the two emergence angles are shown for all deflections of an example whisker; the color indicates the assigned direction group. Qualitatively distinct groups are observed for this example and for all whiskers. (*E*) Traces of moments (orange; M_x, M_y, M_z), forces (cyan; F_x, F_y, F_z), rotation angles (magenta; $\Delta\theta, \Delta\phi$), and the spike train observed for three successive deflections are shown for an example whisker/neuron pair. (Scale bars: 0.1 μNm, 0.5 μN, and 5°, respectively.)

Most Neurons Are Jointly Tuned to Direction and Location of Stimulation along the Whisker Arclength. Previous studies demonstrated that the Vg firing rate is strongly influenced by both deflection direction (2, 10, 12, 31–33) and the arclength of stimulus contact (4, 28). However, these studies have not quantitatively examined the joint effect of these parameters. We quantified the effects of simultaneous changes in both arclength of contact (two or three groups) and direction (eight groups) (see *SI Appendix*, *Extended Methods*: Identification of direction and arclength groups for details on group definitions). For each neuron, we computed

the average firing rate across many deflections for each arclength/direction combination and used it to compute a directional selectivity index (DSI) defined as $(1-\sigma^2)$, where σ^2 is the directional circular variance (34) (*SI Appendix*, *Extended Methods*).

The results of this analysis are shown in Fig. 2 *A–D* for one example neuron. This neuron's firing rate increased as stimulation became increasingly proximal (Fig. 2 *A* and *C*; two-way ANOVA F = 509 main effect of arclength, $P < 0.001$; Tukey's post hoc test $P < 0.05$). The neuron's preferred direction was near 225° (Fig. 2 *B* and *C*; F = 305 main effect of direction, $P < 0.001$; Tukey's post hoc test: $P < 0.05$ for 22/28 multiple comparisons), and it exhibited a moderate DSI (0.54 for proximal stimulation, 0.64 for distal stimulation) (Fig. 2*D*). For each cell, the DSI was calculated by bootstrapping; we randomly sampled half of all contacts without replacement for 1,000 replicates to compute the mean DSI and its SD. The example neuron was more directionally tuned for distal contacts (Student's *t* test: t = 123, $P < 0.001$). Notably, multiple combinations of arclength and direction can result in the same firing rate (Fig. 2*C*).

These results are generalized over all neurons in Fig. 2 *E* and *F*. Of the 78 recorded neurons, 75 had distinguishable arclength and direction groups. Although all 75 neurons exhibited significant direction tuning (two-way ANOVA $P < 0.05$), the DSI was continuously and uniformly distributed across all neurons (Fig. 2*F*; Kolmogorov–Smirnov test: $n = 75$, D = 0.068, $P = 0.88$), revealing a continuum of directional tuning strength across the population. Nearly all neurons (72/75) were also tuned for arclength, with proximal stimulation typically evoking stronger responses.

Importantly, the firing rate of most neurons (68/75, two-way ANOVA, $P < 0.05$) was modulated by both direction and arclength. Fig. 2*G* shows the change in DSI for distal compared to proximal stimulations for the 68 cells that were significantly tuned for both direction and arclength. Cells with ($DSI_{distal} - DSI_{proximal}$) greater than zero were more directionally tuned for distal contacts (28/68 neurons). Note that approximately equal numbers of neurons become more/less directionally tuned as stimulation became increasingly distal. This result indicates that the arclength of stimulation has no consistent effect on direction selectivity, and thus, there is no clear evidence to support increased angular sensing resolution for either proximal or distal stimuli.

The results of Fig. 2 indicate that the more naturalistic, complex stimulation used here can recapitulate classical Vg responses observed during controlled ramp-and-hold stimulation (3, 9, 10). Fig. 2 also accentuates an underappreciated characteristic of Vg responses: when direction and arclength covary continuously and simultaneously, as during natural contact, Vg firing rate is governed jointly by both parameters. These results suggest that a single neuron's response cannot unambiguously encode either of these two stimulus features and that a population readout is required to disambiguate.

Temporal Patterns of Spikes during Contact Are Complex and Direction Dependent. The previous analyses characterized average Vg firing rates, but detailed temporal features of Vg spike patterns are important in shaping central responses (35). We exploited variability across individual deflections to quantify the dependencies between temporal firing pattern and deflection direction across cells (Videos S1–S3). Two examples are shown in the time-normalized histograms of Fig. 3*A*. Cell 1 exhibits strong changes in average firing rate with stimulation direction, with no change in temporal firing pattern. In contrast, the firing pattern of Cell 2 varies significantly with stimulation direction; some directions

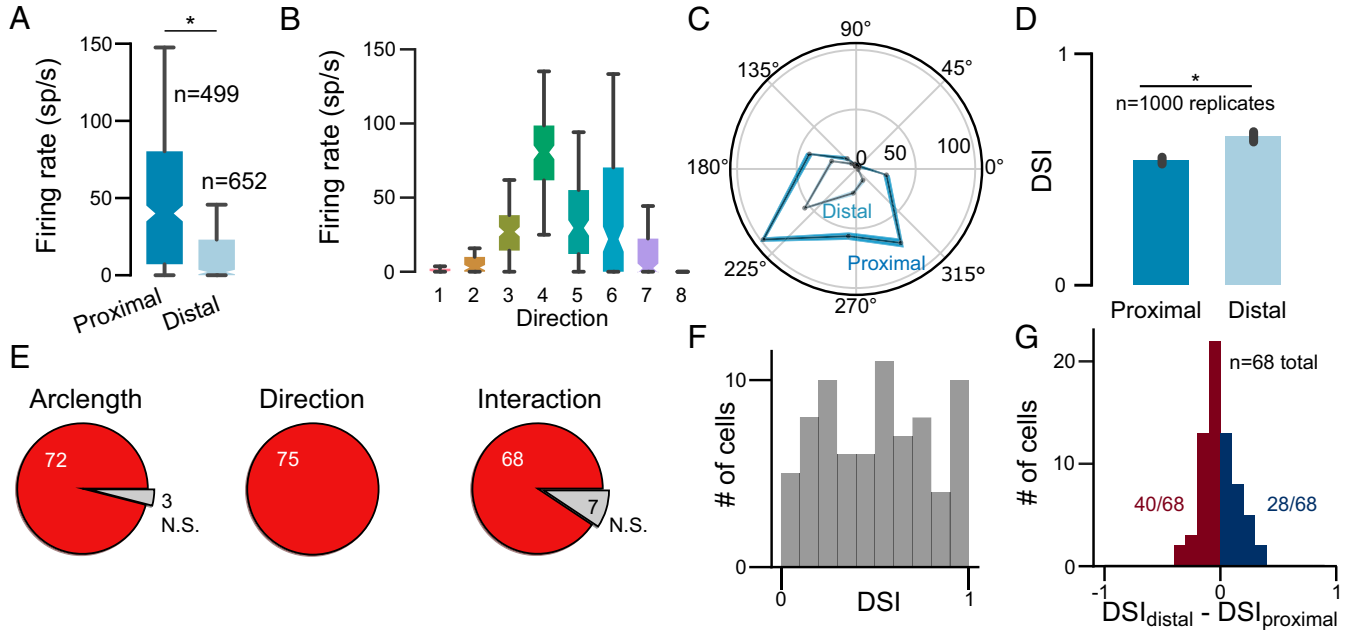

Fig. 2. Most neurons have firing rates that correlate both with arclength of contact and deflection direction: (*A–D*) An example neuron whose firing rate is modulated by both arclength and direction. In *A* and *B*, boxes are median ± 1 quartile and capped lines are median ± 2 quartiles. (*A*) Firing rate increases as stimulation becomes more proximal (*$P > 0.001$). (*B*) Firing rate modulation by direction group. The DSI for this neuron is 0.72. (*C*) Average firing rate and directional selectivity can depend on the arclength of contact. The average firing rate of the example cell is shown as a function of deflection direction for both the proximal and distal arclength of contact. The lines indicate the average firing rate for all deflections in each group, with line thickness indicating ± SEM. Note that for this neuron, the directional tuning curve is broader for more proximal stimulation, indicating a weaker directional tuning for more proximal deflections. (*D*) Quantification of the DSI for the example cell. Bar is mean ± SD (*$P < 0.001$). (*E*) Number of cells with significant effects of arclength, direction, and their interaction on firing rate (two-way ANOVA). Red indicates significant effects. (*F*) Vg neurons range from not at all directionally modulated (DSI = 0) to very strongly modulated (DSI = 1). (*G*) Directional tuning strength is modulated by arclength of contact for most cells. Cells with positive ($DSI_{distal} - DSI_{proximal}$) are more directionally tuned for distal contacts (28/68 neurons).

show a strong onset response, others a strong offset response, and yet others show neither.

The center plots in the two examples of Fig. 3*A* show time-varying firing rates as grayscale heat maps for each direction, with the times of maximal firing rate ("peak times") indicated by yellow asterisks. The peak times for all cells and directions are shown in Fig. 3*B*. Each cell has eight peak times, one per direction. Cells are ordered by peak time variance; cells with little directional modulation of peak time are at the top and those with strong modulation at the bottom. Fig. 3*C* aggregates data across neurons and directions; peak times are most likely to occur at onset, less likely at offset, and least likely in the middle of deflection. The influence of deflection direction on the peak time was quantified with the DSI of the peak time; Fig. 3*D* shows that the DSI of peak time is normally distributed (Shapiro test: n = 77, W = 0.98, P = 0.49). Deflection direction has a moderate influence on spiking patterns, with few neurons very strongly (DSI ≅ 1) or very weakly (DSI ≅ 0) modulated.

Vg neurons are frequently classified as rapidly adapting (RA) or slowly adapting (SA) based on their response to ramp-and-hold stimulation (3, 9–11, 32). To perform a similar analysis with the present data, we introduce an "adaptation index" (AI) as the log ratio of the firing rate during the first 10 ms of contact to the average firing rate. The AI is calculated separately for each direction group. An AI of zero indicates no difference between onset firing rate and mean firing rate; a strongly negative AI indicates almost no firing during onset. The AI for each deflection direction of Cell 2 is shown in Fig. 3*E* and aggregated for all neurons and directions in Fig. 3*F*. Cells are ordered by the mean value of AI across all directions. Note that cells which spike preferentially at onset (*Top*, red cells, "RA-like") transition smoothly into cells that spike less during onset than average (*Bottom*, blue cells; "SA-like"). This smooth transition is maintained if only the preferred direction (PD) of each neuron is considered (Fig. 3*F*, right column).

Consistent with previous studies (33), Vg adaptation properties often depend strongly on deflection direction; some cells exhibit positive AI for some deflection directions and negative AI for others. Previous work classified each neuron into an "adaptation category" based on the number of directions in which it responded in an RA-like manner (33). Similarly, we defined a neuron to be RA-like for a given direction if the AI for that direction is positive. The number of directions for which a neuron responds in this RA-like manner is termed its "adaptation category"; cells are almost evenly distributed across adaptation category (Fig. 3*G*).

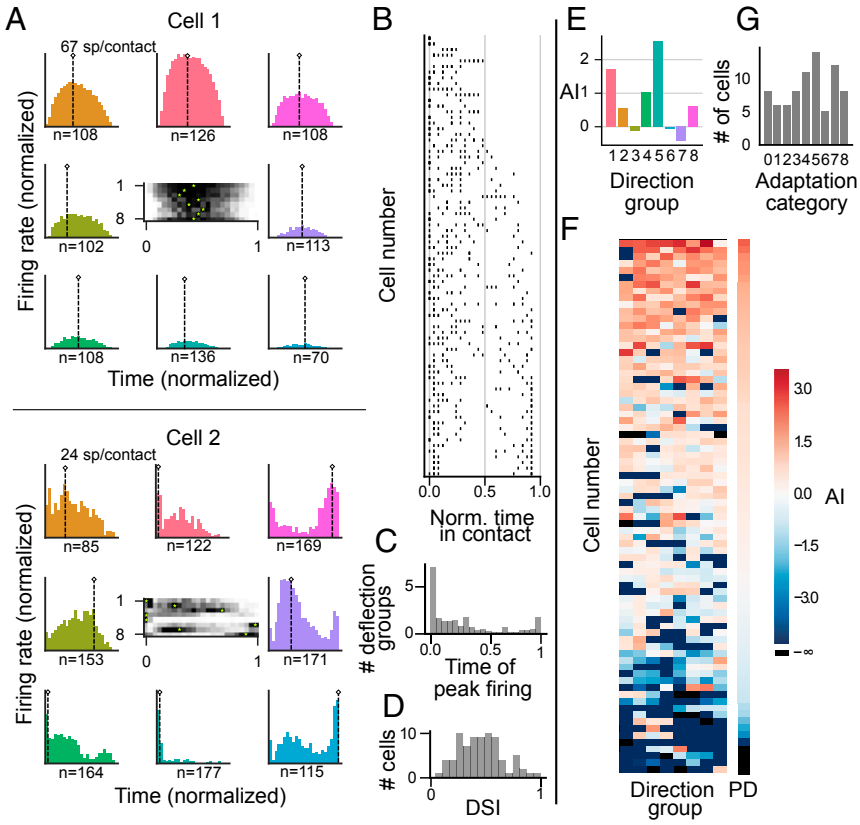

Fig. 3. The temporal structure of Vg responses can be complex and direction dependent. (*A*) Normalized peristimulus time histograms (PSTHs) grouped by deflection direction for two example neurons. Horizontal axes are normalized to a contact duration between 0 and 1. Vertical axes are scaled up to the neuron's maximum firing rate; direction groups are color coded as in Fig. 1*D*. Color, position, and number denote direction group of the PSTH. The number of contacts (n) used to construct each PSTH is indicated below each horizontal axis. Cell 1 shows little change in temporal pattern with deflection direction, while Cell 2 shows significant modulation. Central plots show the eight histograms; *y*-axis indicates direction group. Firing rate is shown in grayscale; a yellow asterisk indicates peak firing rate, which can occur between contact onset (time = 0) and offset (time = 1). (*B*) Time of peak firing rate(s) for all neurons in all directions. Each row represents a neuron; each row has eight points, one for each direction group. Identical peak times for several directions appear as superimposed points. Cells are ordered by variance of peak time of firing. (*C*) Histogram of time of peak firing collapsed across neurons and directions. (*D*) DSI of peak time as a function of direction across neurons. If peak time is heavily modulated by direction, DSI ≅ 1. (*E*) AI for each direction for Cell 2. (*F*) AI for all neurons and direction groups. Cells are ordered by mean AI across all eight directions. Right column (PD) isolates the AI for each neuron's preferred direction, ordered by decreasing AI. (*G*) Adaptation category for all cells.

Neural Responses Are Correlated with Many Stimulus Components, but These Stimulus Components Are Tightly Correlated. The 3D whisker shape and rotation measured from video can be used to model the mechanical signals at the whisker base. Decomposing the forces and moments into their x, y, and z components yields six quantities, while the two angular rotations, $\Delta\theta$ and $\Delta\phi$, are proxies for the forces associated with the follicle rotating within the tissue. These eight quantities and their derivatives form a total of 16 dimensions that completely describe the whisker's mechanical state at its base. A tuning map from this 16-dimensional input space onto the average firing rate of each neuron quantifies the neural response during contact. The full tuning map for each neuron can be projected onto each individual input dimension; some of these one-dimensional tuning maps (tuning curves) are shown in Fig. 4*A* for an example cell, and additional 2D tuning maps are shown in Fig. 4*B*. The total number of spikes in these histograms is 11,010; bins in which fewer than 10 observations occurred were omitted from the maps.

Generally, tuning curves for all cells showed structure in most of the one-dimensional projections: the firing rates of most Vg neurons correlate with most individual parameters. However, these correlations could result from intrinsic covariation between individual stimulus components—for instance, M_y covaries with dF_z, where d is the distance from the whisker base to the contact point. To quantify these covariations, we performed principal component analysis (PCA) on the input space for each whisker (with and without derivatives); the cumulative percent variance explained is shown in Fig. 4*C* for all whiskers.

The PCA allows us to investigate whether neural responses encode the eigenvectors, that is to say, the covariance structure of the mechanical stimulus space. Instead of using the physical quantities as independent variables, tuning maps can also be obtained along stimulus space directions determined by the principal components (PCs) of the input space. Example low-dimensional tuning maps for the two first PCs are shown in Fig. 4*D* for the same neuron as in Fig. 4*B*. Derivatives are included in the PCA decomposition; notably, PCA eigenvectors tend to represent combinations of either physical quantities or their derivatives but rarely mix both (*SI Appendix*, Fig. S3).

We next use PCA to ask whether the deformation of different whiskers across the pad results in exploration of similar or dissimilar subspaces of the overall mechanical space; that is, are all whiskers constrained to explore particular combinations of mechanical variables and their derivatives? If so, such constraint would likely be due to shared biomechanical and morphological properties across whiskers. Because all physical quantities are measured independently of the whiskers' orientation on the head (36), we can quantify the similarity between the leading low-dimensional PC representations of stimuli space across different whiskers. We used a similarity metric (S_i) that generalizes the dot product to measure the angles between two subspaces rather than the angle between two lines (*SI Appendix*, *Extended Methods*: Similarity metric). This approach is formally known as "canonical angles analysis" ($S_i = \cos(\xi_i)$) (37) and resembles the "subspace overlap" used in previous work (38). Lines are one-dimensional; there is only one angle between two lines. In general, there are as many angles, or similarity metrics S_i, as dimensions in the subspaces being compared. A value of $S_i = 1$ corresponds to two parallel lines, one within each subspace, indicating high similarity in orientation between the spaces. A value of $S_i = 0$ corresponds to orthogonal directions. Multiple angles between subspaces are ordered by decreasing S_i (i.e., increasing ξ_i).

We quantified input space similarity across whiskers by computing $S_i, i = 1,2,3$ for pairwise comparisons between all stimulated whiskers based on the subspaces spanned by the first three PCs for each whisker (Fig. 4*E*). Because the applied stimulation varied with each experiment and because the mechanical properties of each whisker are unique, the explored mechanical stimulus space is also unique, even for experiments on whiskers that have the same row and column identity. Most pairwise comparisons were found to be similar: $S_i > 0.82 > 0.54 > 0.05$ for 95% of the three leading angles. These values identify similarities across two of the three dimensions; weak clustering occurs only for the third canonical angle. This result implies substantial similarity of the relevant input space across whiskers and allows us to compare neural tuning properties across neurons innervating different whiskers.

Generalized Linear Models Reveal Encoding of Rotation and Distributed Tiling of Explored Stimulus Space. The preceding sections have shown that Vg neurons encode multiple stimulus features and that stimulus features themselves are strongly correlated. The one- and two-dimensional tuning maps of Fig. 4 *A* and *B* provide intuition for the neural representation of select stimulus features but fall short of describing the full neural response to the presented stimuli. A full description would require knowing the average firing rate in response to any arbitrary point in the stimulus space and thus fitting a tuning histogram such as those in Fig. 4*A* to the full 16-dimensional stimulus space. This goal cannot be achieved by systematic and exhaustive exploration and requires a modeling approach.

We therefore implemented a recent formulation of generalized linear models (GLMs) (25) that allows for multiple input filters and thus for the activity of modeled neurons to be triggered by inputs in multiple directions within the stimulus space. All models were fit with three filters, each defined in the 16-dimensional input space (see *Methods* and *SI Appendix*, Fig. S4). Only stimulus values at the current time bin were accessible to the models, which included no input history. Spike history terms were omitted from the model because their inclusion frequently resulted in the "runaway firing" of model neurons (see *Methods*). A parametric cylindrical nonlinearity (five parameters) was applied to each term in the sum of the three filters (see *Methods*), bringing the number of model parameters to $[(16 + 5)*3] = 63$ per neuron; overfitting was minimized via 10-fold cross-validation.

As illustrated for the example neuron in Fig. 5*A*, we used the models to predict a time-varying spike rate with millisecond resolution, then smoothed the observed spike train with a Gaussian kernel whose SD σ was varied exponentially from 2 to 512 ms, and finally compared the predicted rate to the smoothed rate for each value of σ. The Pearson correlations comparing the observed and predicted rates are shown in Fig. 5*B*; correlations are calculated only during contact periods. On average, models best predicted the observed spike rate for $\sigma = 32$ ms, but for many neurons, high prediction accuracies were achieved for σ as short as 2 ms. Moreover, performances achieved with $\sigma = 16$ and 8 ms were statistically indistinguishable from that achieved for $\sigma = 32$ ms (Tukey's post hoc test). The relationship shown in Fig. 5*B* is nonmonotonic; model performance drops as the value of σ increases, indicating that the models accurately predict high-resolution temporal structure in the spike trains rather than fitting the average spike rate. The median correlation value was 0.69 (IQR = [0.55, 0.81]) for $\sigma = 32$ ms, with a minimum = 0.08 and a maximum = 0.91.

To determine how much information is gained from the full 3D whisker shape compared to a 2D projection (Fig. 5 *C* and *D*), the 3D whisker shape was projected into the top camera view. The four mechanical variables associated with contact, $\{M, F_x, F_y, \Delta\theta\}$, were computed using an established 2D model (24, 39). We mapped this eight-dimensional input space (including derivatives) onto the average firing rate of each neuron and, as in the 3D case, modeled each map using a GLM with three filters. A total of 70 neurons were fit with both 2D and 3D models. We again found that the accuracy of firing rate prediction was nonmonotonic with the value of σ used to smooth the observed spike trains. For $\sigma = 32$ ms, 2D model performance was significantly worse than that of 3D models (Wilcoxon signed-rank test, W = 51.0, $P < 0.001$; median = 0.48, IQR = [0.37, 0.60]). When the 3D model for a given neuron is compared with its 2D counterpart, nearly all models (60/70)

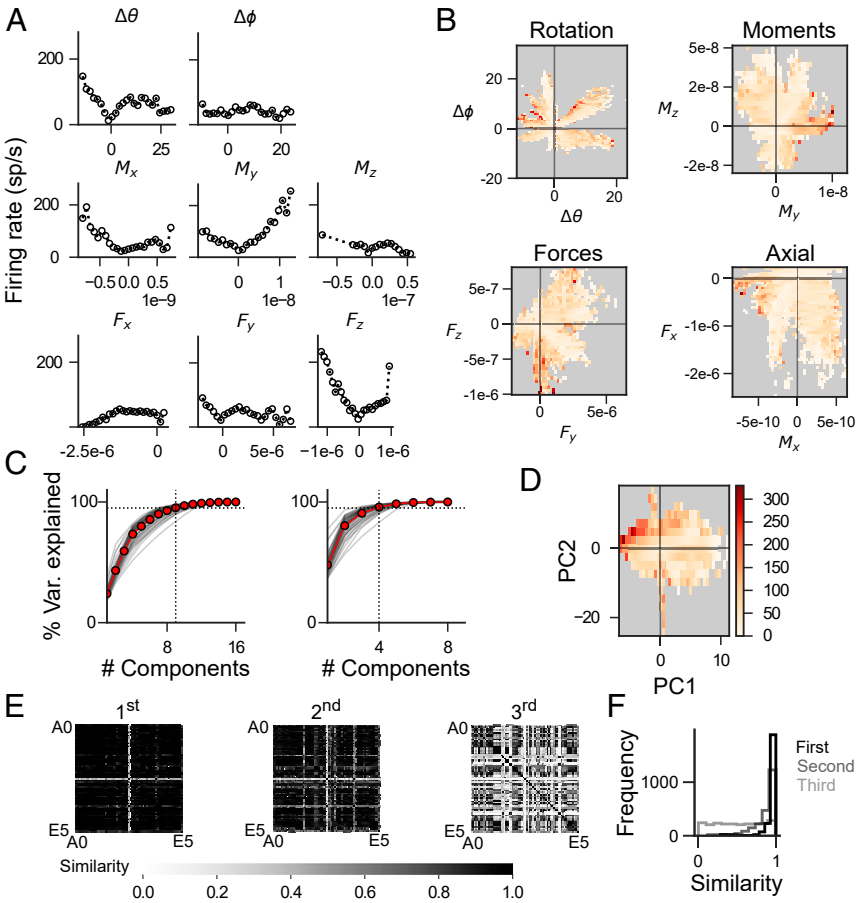

Fig. 4. State spaces for each whisker fall in a lower dimensional subspace. In *A*, *B*, and *D*, the number of spikes comprising the histograms is 11,010. (*A*) One-dimensional tuning maps: firing rate as a function of individual components of bending and rotation for an example cell. Units are degrees (*Top*), Newton meters (*Middle*), and Newtons (*Bottom*). (*B*) 2D tuning maps: firing rate as a function of pairs of components for the same neuron as in *A*. The color indicates firing rate with the scale as in *D;* axes units as in *A*. Bins in which fewer than 10 observations occurred were omitted from the map. (*C*) The cumulative percent variance explained by subsequent additions of ordered PCs for all whiskers (gray) and on average (red) when derivatives are included (*Left*) and excluded (*Right*). A 95-ms window locally estimated smoothing (LOESS) was used before the derivatives were computed. Dashed horizontal lines indicate 95% variance explained threshold; vertical lines indicate the number of components needed to exceed the 95% threshold. Without the derivatives, three components are required to explain 95% of the variance in the eight-dimensional space; with derivatives, eight components are required to account for 95% of the variance in the 16-dimensional space. (*D*) 2D tuning map of the neuron in *B* for the two first PCs of its input space, which includes derivatives. (*E*) Pairwise comparisons of the similarity between the 3D subspaces spanned by the first three PCs for all whiskers. Axes are ordered by whisker identity (A0(α) – E5). Multiple whiskers of the same row and column identity were included because whisker geometry differs across rats, and stimulation pattern differs across trials. Shading is the value of $S_i = \cos(\xi_i)$. (*F*) Histogram of the number of pairwise comparisons with a given value of $\cos(\xi_i)$ for each of the three canonical angles.

perform better with 3D information (Fig. 5*D*). The median performance increase from 2D to 3D was 29.8% (IQR = [13.0%, 73.9%]).

In order to determine the relative contribution of each input component to firing rate prediction, we performed a dropout analysis in which access to information was increasingly restricted (Fig. 5*E*). For these analyses, correlations were computed using only the $\sigma = 32$ ms smoothed rate. Models without derivative information or rotation information perform significantly worse than the full model (Wilcoxon signed-rank test, W = 17, $P < 0.001$, median = 0.61, IQR = [0.52, 0.72]; W = 209, $P < 0.001$, median = 0.55, IQR = [0.43, 0.69], respectively), indicating that these mechanical quantities are important for firing rate prediction.

We then asked how well models performed when given access to only one class of inputs: moments, forces, rotations, or derivatives (Fig. 5*E*). All subsets have access to deflection direction, as the relative contribution of the three spatial components can be used to infer direction. All models with access to only one class perform significantly worse than the full model (Wilcoxon signed-rank test, $P < 0.001$). Models with only rotation components perform only slightly less accurately than the full models (median = 0.68, IQR = [0.52, 0.80], W = 599), indicating that a majority of the variance in firing rates is accounted for by the rotational components of the input. In this anesthetized preparation, the rotational components are indicative of the force the skin exerts on the follicle. In contrast, models with access to only derivatives perform worst of all dropout models (median = 0.47, IQR = [0.36, 0.54], W = 32), while those with access to just moments or forces perform moderately well (median = 0.49, IQR = [0.37, 0.64], W = 31; median = 0.53, IQR = [0.40, 0.67], W = 24). The percent difference $(R_{\text{subset}} - R_{\text{full}})/(R_{\text{full}})$ quantifies whether the loss of either rotation or derivative information is detrimental on a per neuron basis. The results aggregated over neurons (Fig. 5*G*) indicate that some neurons are more amenable to modeling than others and that force and moment both carry important but incomplete information about the response, while rotational variables are the most informative.

Unsurprisingly, models that include derivative information exhibit improved temporal precision. Specifically, models that include derivatives perform better than those that do not when their predictions are compared to spike rates smoothed with $\sigma < 64$ ms

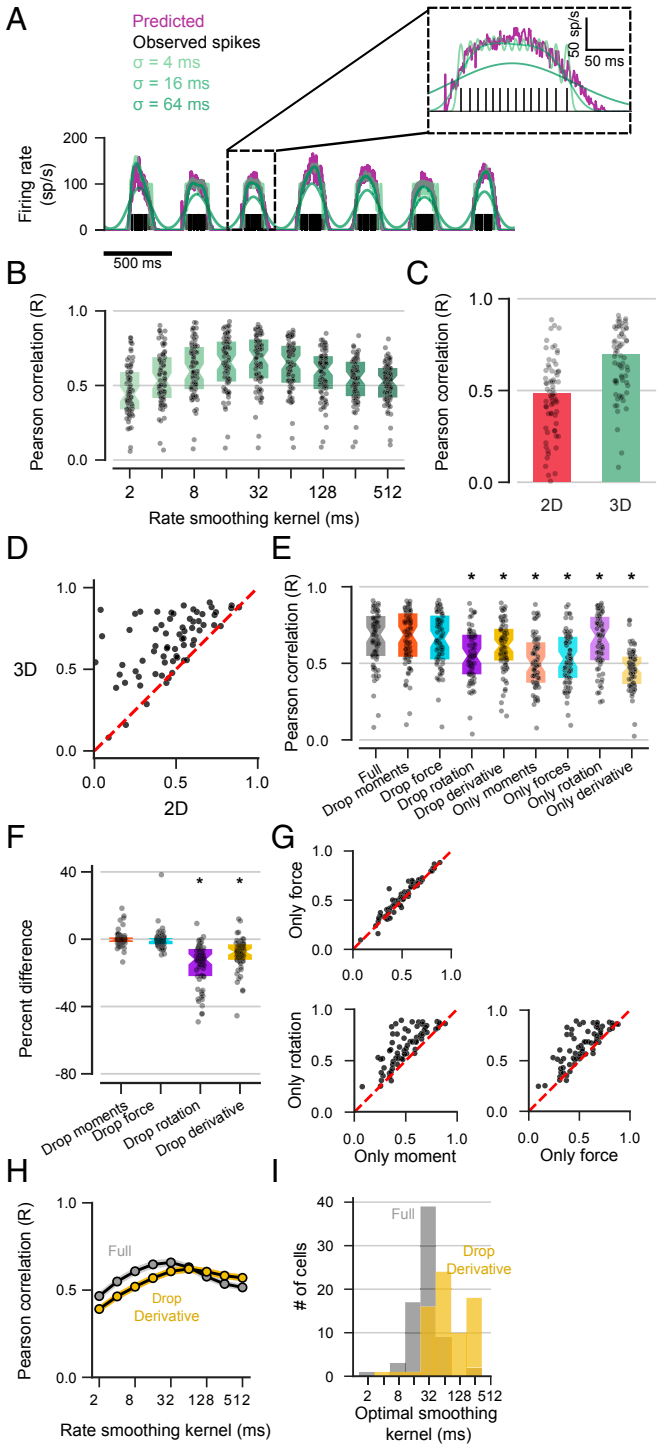

Fig. 5. Statistical modeling of Vg neurons. Dots indicate individual models, bars are medians, and boxes are median ± 1 quartile unless indicated. For all panels except *B*, Pearson correlation values are used to compare predicted firing rate to observed rate smoothed with a Gaussian kernel with $\sigma = 32$ ms. (*A*) Observed spiking (black vertical lines) is converted to estimated rate by smoothing with a Gaussian kernel (green, light to dark: $\sigma = [4, 16, 64]$ ms). Three smoothing resolutions are shown, but nine are computed. The predicted rate is shown in purple. (*Inset*) Single deflection. (*B*) Correlations for GLM-predicted rates compared to the observed spike rates smoothed with Gaussian kernels with increasing σ (light to dark). (*C*) Pearson correlation values for models with access to either 2D or 3D physical information. (*D*) Pairwise comparisons of performance for models based on 2D or 3D physical information. (*E*) Performance of models with access to subsets of the full input space. Asterisk indicates significant difference from performance of full model (Wilcoxon signed-rank test, $P < 0.05$). (*F*) Percent difference between the performance of the full model and the model without access to a subset of inputs, $(R_{subset} - R_{full})/(R_{full})$, aggregated over all neurons. (*G*) Comparison of performance of models with access only to inputs of a single class. (*H*) Comparison of performance of models with and without access to derivatives for rates smoothed with increasing values of σ. Shown are means ± SEM. (*I*) Models with access to derivatives (gray) better predict rates smoothed with lower values of σ than those without (yellow).

(Wilcoxon signed-rank test, $P < 0.001$, Bonferroni corrected for all kernel sizes tested, Fig. 5*H*). Moreover, identifying the value of σ for which the firing rate of each neuron is best predicted shows that most neurons are best predicted at shorter timescales when derivative information is included (Wilcoxon signed-rank test, n= 74, W = 0, $P < 0.001$, Fig. 5*I*).

Lastly, we analyzed the coefficients that characterize the GLM filters. These coefficients are organized as three vectors in the 16-dimensional input space; these vectors define a 3D subspace that can be interpreted as a complex, three-dimensional "mechanical receptive field" for each neuron. This receptive field cannot be visualized using standard tuning curve analyses, but it provides a more complete description of a neuron's response properties and allows us to ask two important questions. First, do these neuron-specific mechanical receptive fields reflect the low-dimensional structure (i.e., the PCs) of the stimulus space associated with the manual deflections used here? And second, how do the mechanical receptive fields of different neurons compare to each other?

Both of these questions can be addressed by computing again the similarity metric S_i based on canonical angle analysis (37). This computational approach is schematized in Fig. 6. For each neuron, we calculated the similarity between the subspace that defines its mechanical receptive field and the subspace that defines the relevant stimuli determined by the deflections applied to the whisker it innervates. Surprisingly, the neural representations are not strongly similar to the PCs: $S_{1,2,3} = [0.36 \pm 0.13, 0.14 \pm 0.07, 0.03 \pm 0.03]$. Fig. 7*A* shows the similarity metrics for all cells, ordered by decreasing similarity. Corresponding histograms are shown in Fig. 7*B*. Thus, Vg neurons do not seem to preferentially encode the mechanical stimuli that lie in the subspace spanned by the leading eigenvectors.

We next calculate the similarity between the neural representations of different neurons to determine if there are identifiable "groups" or "classes" of neurons that share similar representations. The existence of functional cell classes would be indicated by subpopulations of neurons that are similar to other neurons within their class and dissimilar to those outside their class. Pairwise comparisons are shown in Fig. 7*C* and the resulting histograms in Fig. 7*D*.

In contrast to multiple previous studies that have found distinct Vg cell classes (4, 11, 19, 28, 40, 41), the neural representation subspaces overlap only moderately: $S_{1,2,3} = [0.74 \pm 0.12, 0.45 \pm 0.15, 0.14 \pm 0.11]$, and do not cluster. The lack of clusters and the lack of bimodal distributions in the histograms of the similarity metrics indicate that Vg neurons should not be grouped into classes of cells that represent similar mechanical information.

Thus, the neural representations of Vg neurons do not preferentially cover the relevant subspaces of input space spanned by the leading PCA eigenvectors. Moreover, mechanical receptive fields corresponding to different neurons overlap only moderately and do not cluster. This suggests that as a population, Vg neurons implement a dense uniform covering of the mechanical input space (*SI Appendix*, Fig. S4).

Discussion

Coding properties of Vg neurons can be fully quantified only if the stimuli employed span the extent of the full stimulus space.

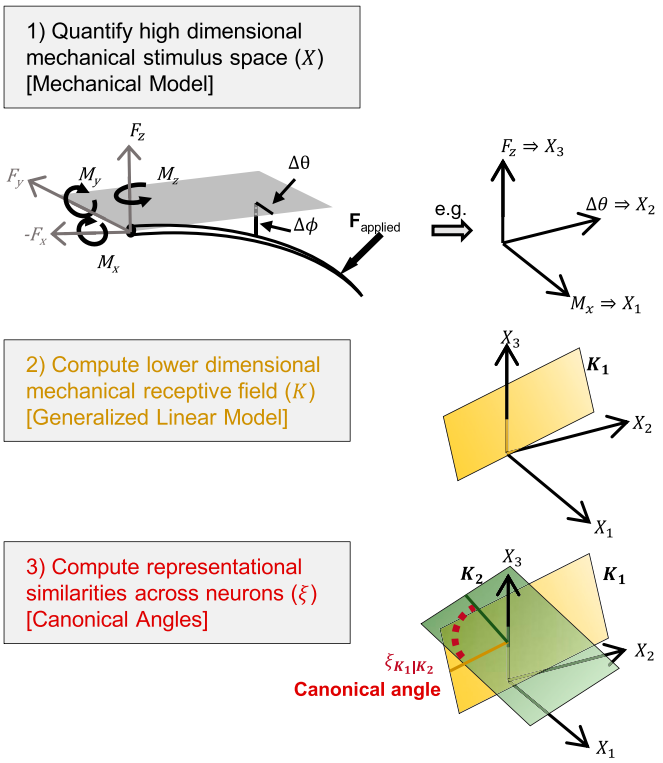

Fig. 6. Mathematical methods schematic: an illustration of the mathematical and modeling methods (*1*). The 3D whisker shape is extracted from each video frame and viewed from a whisker-centered coordinate system. From the 3D whisker shape, we measure the rigid body angular rotations from rest ($\Delta\theta, \Delta\phi$) and estimate the applied force using a 3D mechanical model of whisker bending (24). The applied force can be decomposed into the component forces at the base of the whisker; knowledge of the contact point allows for the computation of component moments. These mechanical quantities and their derivatives define a 16-dimensional stimulus space (X). (*2*) A toy example stimulus space composed of just three dimensions. We fit low-dimensional GLMs to match the observed spiking of each neuron. Each GLM finds a lower dimensional subspace embedded in the higher dimensional stimulus space. This subspace, shown here as the plane K_1 (yellow), provides a representation of the stimuli that explain the firing of the neuron 1 (*3*). We compute the similarities between the neural representations of different neurons by calculating the angles between the corresponding neural representational subspaces (K_1, K_2).

Without claiming to have achieved complete presentation of a naturalistic stimulus space that incorporates the full spatial and temporal structure of natural objects available to an awake animal, the present work takes a significant step toward a more complete understanding of vibrissotactile encoding by relating neural activity to whisker motion in three spatial dimensions. Manual deflection allows the stimulus space to be probed with a previously unexplored degree of variability. This framework allows us to show that individual Vg neurons simultaneously encode multiple features of the stimulus, that adaptation properties do not categorize into RA or SA groups, and that neural representations overlap and tile the stimulus space. Together, these results suggest a view of Vg coding in which single stimulus features cannot be determined unambiguously by the activity of a single Vg neuron; instead, features are represented across a population and may be extracted by more central neurons that integrate information across many Vg neurons. This view contrasts with proposed population codes that segregate behaviorally relevant quantities into separate neural classes (11, 28, 40, 42).

Classical Vg Tuning Curves Are "Slices" of Possible Neural Responses to Complex Stimuli. Previous studies used restricted stimulus sets that vary only a few stimulus dimensions while holding others constant (1–3, 7, 9, 10, 32). The Vg responses shown in these earlier studies can be considered "slices" through multidimensional tuning maps that more completely describe responses to complex stimuli.

In agreement with earlier work (9, 10, 28, 33), our results show that both arclength of contact and deflection direction strongly influence average firing rate. Here, we further show that Vg neurons are jointly tuned to both stimulus features, that is, arclength and direction cannot be disambiguated based on the average firing rate of single Vg neurons (Fig. 2). We use extended GLMs to describe these more complex tuning maps from which general coding principles can be inferred. For instance, the predictive performance of these models decreases when derivatives of mechanical features are omitted as inputs (Fig. 5*E*), consistent with earlier work showing joint tuning to features corresponding to stimulus "amplitude" and "velocity" (1–3, 7, 31, 32).

Recent studies based on 2D analyses of whisker shape under deflection have shown that Vg responses are more accurately described in terms of mechanical rather than geometric variables (18, 19, 29), but the 2D work omits crucial information about a third deflection direction that modulates the components of the forces applied at the base of the whisker. The Vg responses shown in these 2D studies can thus also be considered as "slices" or projections of responses to the 3D stimulation used here. The marginal neural responses to individual features of the stimulus obtained here recapture observations from previous work; however, a more complete picture emerges when responses to more multidimensional stimuli are analyzed without marginalizing to individual stimulus features.

Vg Neural Responses Tile the Mechanical Space. Vg responses are tuned to multiple features of the 3D mechanical stimulus space (Fig. 5); statistical models indicate that their activity is primarily driven by the follicle's rotation in the skin rather than by whisker bending. The predictive performance of the Vg models degrades if information about rotation is omitted but does not degrade if information about bending is omitted. Remarkably, models that have access only to bending information still perform moderately well, providing evidence for broad and diffuse tuning to mechanical features.

Given the relationship between bending and rotation (*SI Appendix*, Fig. S1), it is possible that neurons encode latent mechanical features that subsume bending and rotation. PCs of the stimulus space represent such latent combined features. However, the neural representation of stimuli that maximally triggers Vg activity does not align strongly with the PCs of the stimuli (Fig. 7); neurons do not encode linear combinations of stimulus features along high variance dimensions. Preferential encoding along dimensions that differ from those that characterize the variance structure of the stimuli is consistent with a diffuse tiled representation of mechanical information.

Although the present work used passive whisker deflections, we expect the neural coverage of the stimulus space explored here to remain stable regardless of whether exploration is active or passive. The representation of a stimulus by a Vg neuron cannot depend on context, as the Vg contains no interneurons and receives no descending inputs. However, a Vg neuron's response will depend strongly on the particular mechanical stimulus, and thus the overall description of Vg activity will be strongly affected by the range and statistics of the stimuli used. In the present study, neural responses are likely dominated by rotations of the whisker–follicle complex because the muscles holding the whiskers are relaxed as the animal is anesthetized. During active whisking, the muscles contract around the follicle, resisting passive rotation within the skin and causing the whisker to bend rather than rotate (18, 43). In

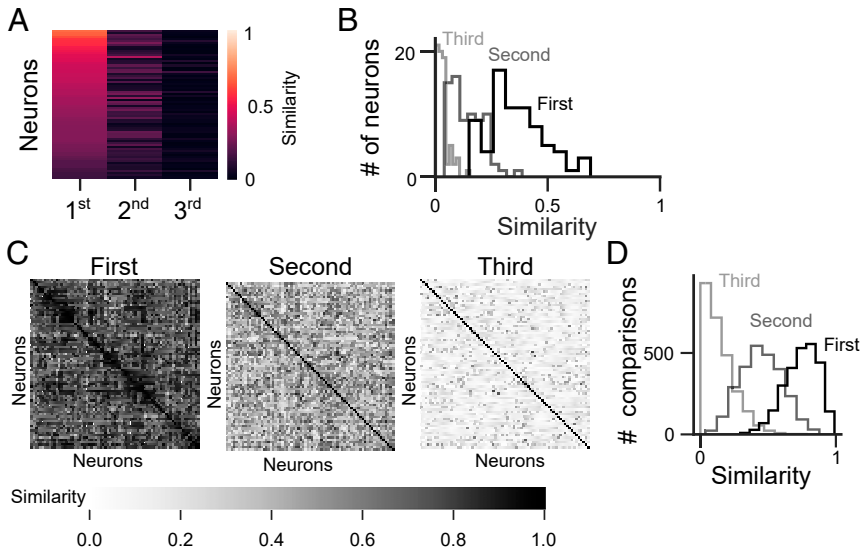

Fig. 7. Neural tuning is well distributed across the population and covers the input space. (*A*) The similarities $S_{1,2,3}$ between the stimulus subspace spanned by the three leading PCs and the 3D representation of the neural receptive field are shown for each neuron. The value of S_i between the input subspace and the neural subspace is color coded (scale, *Right*). Each row is a neuron; neurons are ordered by the value of the first canonical angle. (*B*) Histograms of the values of $S_{1,2,3}$ over all neurons. (*C*) Pairwise similarities of neural representations across all recorded neurons. Axes are ordered as determined by Ward hierarchical clustering to group similar neurons. Gray intensity (scale on bottom) indicates the similarity value S_i. (*D*) Histograms of the values of $S_{1,2,3}$ across all pairwise comparisons of the neural subspaces.

addition, increases in blood pressure in awake animals will tend to stiffen the follicle near the ring sinus, increasing the effects of the whisker's deformation (44, 45). These differences in mechanical signals will affect the stimulus space; for the awake animal, bending is likely to be more prominent during active whisking. However, the neural representation of the mechanical space itself ought to remain unchanged. More central neurons could extract features of the stimulus from a tiled and distributed representation in the Vg population while accounting for the invariance of the map from stimulus space to Vg neural activity across passive and active contexts.

Adaptation Characteristics of Vg Neurons Lie along a Continuum. Vg neurons are typically classified as RA and SA. This classification is conceptually intuitive, simplifies analyses, and is consistent with the existence of genetically and physiologically distinct mechanoreceptor types (46–48). However, during the more naturalistic stimulation used here, we observe a continuous distribution of adaptation properties that depend on direction (Fig. 3). This finding supports earlier interpretations of noncategorical adaptation responses (12, 32, 33).

One interpretation of this finding is that Vg neurons respond both to mechanical features and their temporal derivatives with differential weights, such that some neurons respond very little to derivatives (SA-like) and others exclusively so (RA-like). The precise balance of these weights is likely affected by various aspects of follicle configuration: the physiological class of the mechanoreceptors, the arrangement and location of the mechanoreceptors in the follicle, and the tissue dynamics of the follicle/mystacial pad (43, 49). The diversity within and across classes of mechanoreceptors likely generates diverse responses in the Vg population, resulting in a more complete tiling of the possible stimulus space and thus avoiding gaps in the information conveyed to more central neurons (50, 51).

On the Plausibility of a Dense Code. To fully describe the trigeminal population code would require simultaneous recordings from many Vg neurons. In this study, Vg neurons were individually and sequentially recorded from different animals. Nonetheless, several lines of reasoning suggest that the most parsimonious interpretation of the present results is that the population of Vg neurons represents the stimulus space via a dense or nearly dense code.

First, each Vg neuron responds to many different mechanical states of the whisker (Fig. 5) and to many stimulus features (Fig. 2); many Vg neurons are thus required to fully represent any given stimulus and any given stimulus feature. Second, Vg coding properties are continuously distributed across all recorded neurons (Figs. 3 and 7). Direction selectivity index, temporal adaptation patterns, alignment of the neural representation with the stimulus PCs, and alignment between neural representations all vary smoothly across the entire population of recorded neurons, indicating a tiling of the input space. Finally, Vg neurons exhibit a wide range of firing rates (Fig. 2) (12, 16, 32) consistent with a dense coding scheme (52).

Vg neurons must represent a large range of mechanical stimuli in multiple behavioral contexts, including active and passive touch, texture discrimination, collisions with objects, noncontact whisking, and airflow exploration (19, 53–55). Although it is not possible to sample all whisker velocities and vibration patterns, the present work leverages manual stimulation and stereo videography techniques to explore and quantify a vastly larger stimulus set than previously reported. It will be crucial for future work to determine how the tuning properties of these neurons encode dynamic interactions with complex objects that give rise to fine-scale deformations such as slip-stick events and texture exploration; it remains to be seen how Vg neurons achieve robust encoding under such varied contexts and behaviors. We quantified the 3D motion of the whisker during deflections applied at multiple locations along the whisker length and with larger displacement angles than previous passive stimulation experiments. This approach allowed us to analyze Vg responses to deflections that occur during natural exploration but are mostly impossible for a head-fixed animal, such as dorsal ventral deflections.

Future studies may investigate how the encoding properties described here coexist with Vg neurons' ability to encode texture and self-motion. A dense coding scheme such as the one proposed here would offer several distinct advantages. It is robust to noise in individual neurons and to neuronal loss. It has a high

representational capacity, a useful property given that there are only about 200 to 300 Vg neurons per whisker (56). A distributed dense code would allow for individual Vg neurons to be informative of stimuli under different contexts, without filtering out information at this early stage. In this way, the Vg population could represent arbitrary stimuli in the space of all possible stimuli and allow for more central neurons to extract those features that are relevant in the context of the animal's ongoing behavior and motor actions.

Methods

All procedures involving animals were approved by the Northwestern Animal Care and Use Committee. A total of 22 female Long Evans rats between 3 and 6 mo were used. Detailed data processing methods can be found in *SI Appendix*.

Surgical Procedures and Electrophysiological Recordings. Animals were anesthetized with a ketamine–xylazine–acepromazine mixture administered intraperitoneally (60.0 mg/kg ketamine, 3.0 mg/kg xylazine, and 0.6 mg/kg acepromazine). After deep anesthesia was induced, the fur from the left whisker array was removed with depilatory cream (Nair) to increase contrast near the proximal region of the whisker close to the basepoint. Care was taken to minimize contact between Nair and the whiskers and to wash off the Nair as soon as possible with saline. If the shape of a whisker was visibly altered by the fur removal procedures, it was removed from the array prior to recordings.

The head was immobilized with ear bars to a custom stereotaxic device, and three stainless steel skull screws were inserted on the dorsal aspect of the cranium. Prior to the surgery, a noninsulated silver wire had been soldered to one of the skull screws to serve as a ground wire for electrophysiological recordings.

An ∼1 mm diameter craniotomy was made over the left hemisphere, 2 mm caudal to bregma and 2 mm lateral to the midline. The skull was leveled to ensure that the bregma–lambda plane was horizontal, and a dental cement (methyl methacrylate) "bridge" was formed to connect the skull screws to the right side of the stereotaxic device. This procedure allowed for removal of the bite support and left ear bar while maintaining a level head position, giving free access to the left whisker array for stimulation. Once the dental cement bridge had set, a single tungsten electrode (FHC 1 to 3 MΩ) was centered over the craniotomy and lowered to a depth of ∼10 mm, until whisker-responsive field potentials could be heard in audio monitoring of the amplified electrode signal during manual stimulation of the entire whisker array. We then waited ∼5 to 10 min to allow the brain to relax after the initial penetration before advancing slowly to isolate a unit that responded only to the deflection of a single whisker.

Once a single unit was isolated, the whisker associated with that neuron was visually isolated to ensure high contrast in both front and top camera views. A white paper background was placed behind the whisker to provide a uniform background for robust tracking in the front camera. Surrounding whiskers were either trimmed or placed carefully behind the paper background. Care was taken not to deform the whisker of interest or the surrounding mystacial pad.

A custom light-emitting diode (LED) sheet with a transparent white plexiglas diffuser was used as the background lighting for the top camera. An adjustable Neewer CN-160 LED array was used as foreground lighting in the front camera field of view. High-speed video from two identical top and front cameras was recorded directly at either 300 fps (Teledyne Dalsa HM640) or 500 fps (Mikrotron 4CXP) using StreamPix 7. The front and top cameras were synchronized by way of clocked 5V transistor–transistor logic (TTL) to initiate exposure of each frame in both cameras from the same source. At the end of each experiment, we recorded images of a checkerboard pattern with 2-mm squares in the field of view of both cameras; these images were later used for camera calibration and for calculating the 3D whisker shape.

Neural signals were amplified using a A-M systems 4 channel amplifier, with a 10 Hz to 10 kHz hardware filter, at 1,000× gain. Amplified signals were acquired via a Measurements Computing DT304 card using Datawave SciWorks version 8. After acquisition, signals were digitally bandpass filtered at 300 to 6,000 Hz before spike sorting with KlustaKwik (57).

During recording, whiskers were manually deflected with a graphite probe (0.3 mm diameter) in eight cardinal directions with respect to the emerging axis of the whisker. Deflections were applied at two to three distances along the whisker (arclengths), and at approximately two speeds, for a total of ∼32 to 48 different categories of deflection. Each category of deflection was repeated ∼20 times for each whisker. Care was taken to minimize slip along the length of the whisker during a deflection. Neural signals and subsequent stimulus quantifications were analyzed using custom python and MATLAB code based on the neo and elephant python packages.

3D Mechanical Models. The mechanical models used here to calculate the three components of force and three components of moment at the base of the whisker have been described previously (58). All calculations were done in whisker-centered coordinates in which the whisker basepoint is centered at the origin, and the whisker is rotated such that the approximately linear portion of the base segment of the whisker is colinear with the x-axis and the initial curvature of the whisker lies in the x-y plane. Mechanical models take the 3D shape of the whisker in the frame prior to each contact onset as the reference whisker for that contact. In each subsequent contact frame during which the whisker is deformed, we estimated the forces and moments required to deform the reference whisker into the whisker shape observed during contact.

As described in previous studies (24, 39, 58), the mechanical model approximates the whisker as a tapered, truncated beam. The three components of force and three components of moment $\{F_x, F_y, F_z, M_x, M_y, M_z\}$ (*SI Appendix*, Fig. S1) were computed at the base of each whisker. Importantly, these computations were performed in whisker-centered coordinates for each frame so that the applied force takes into account only the change in shape of the whisker (i.e., bending). To calculate the rotational component during whisker deflection, we computed the rotation (θ, ϕ) required to move the whisker from the camera-centered reference frame to the whisker-centered reference frame at every point in time. The rotation magnitude in each frame was then computed as the change in these angles $(\Delta\theta, \Delta\phi)$ from the position of the whisker in the frame prior to contact. Marginal distributions of mechanical and kinematic variables are shown across all contacts and whiskers in *SI Appendix*, Fig. S2.

In some cases, we used two additional scalar quantities: the magnitude of the bending moment M_B and the rotation magnitude M_R, which quantifies the arc swept in the direction of rotation:

$$M_B = \sqrt{M_y^2 + M_z^2},$$

$$M_R = \sqrt{\Delta\theta^2 + \Delta\phi^2}.$$

2D Mechanical Models. In order to assess the amount of information gained when moving from 2D to 3D, we calculated the mechanics resulting from the bending and rotation of the whisker as if we only had information from the top camera. Since the reconstruction of the 3D whisker is an estimation of the 3D shape, it was inappropriate to simply compare the 3D information with the information obtained from direct 2D tracking from the top camera, as the latter is likely more accurate. Instead, we back projected the estimated 3D whisker onto the top camera to get a 2D image of the whisker of comparable quality to that of the 3D reconstruction. The contact point was the same node along the whisker as identified during the 3D analysis and did not need to be recomputed. We used the back-projected 2D whisker shape to calculate the angular rotation $\Delta\theta$ as for the 3D models but now restricted to the 2D projection. We then applied a previously described 2D mechanical model (59, 60), analogous to the 3D model already discussed, to calculate the bending magnitude M, the axial force F_x directed into the follicle, and the lateral force F_y. The derivatives of these physical quantities were calculated as described for the 3D mechanical quantities. The resulting eight-dimensional stimulus space included $\{M, F_x, F_y, \Delta\theta\}$ and their respective derivatives.

Low-Dimensional Tuning Maps. Similar methods were used to calculate tuning maps in one and two dimensions. In one dimension, the stimulus variable was binned into 25 equal bins; in two dimensions, each of the two stimulus variables was binned into 50 equal bins. The resulting histograms sample the prior probability distribution of the stimulus marginalized to the corresponding one or two dimensions within the 16-dimensional stimulus space. Bins for which the corresponding stimulus value was observed less than 10 times were considered empty. For occupied bins, normalized counts were used to estimate the prior probability distribution of the stimuli.

The evoked firing rate of the neuron being mapped was then computed for all occupied bins. The time-dependent spike rate was estimated by convolving the binary spike train with a Gaussian kernel with $\sigma = 2$ ms. For such small σ, conversion to a rate provided smoothing without greatly altering the temporal information. These rates were used to create a new

histogram that estimated the expectation value of the firing rate given the stimulus. To this end, an average spike rate for each stimulus bin was computed over all the times a stimulus value within that bin was observed.

GLMs. The input space available to a model for predicting the firing response of a specific neuron was the 16-dimensional space consisting of $\{M_x, M_y, M_z, F_x, F_y, F_z, \Delta\theta, \Delta\phi\}$ and the temporal derivatives of these quantities. Each input variable was sampled at 1 ms resolution. The target output for training each neuron-specific model was the corresponding binary spike train recorded during the experiment: either a spike was observed (1) or not (0) in each 1 ms bin.

The input $X(t)$ consists of the values of the 16 stimulus variables at the time t of prediction. Since Vg neurons are known to respond to stimulus on fast time scales, sometimes less than 1 ms, and since the temporal resolution of the stimulus is the same as the temporal scale of the Vg response, the model does not need to incorporate a time lag between inputs and outputs or a stimulus history as has been the case in previous applications (29, 61). The models implemented here were constructed using cylindrical basis functions (25):

$$\hat{r}(t) = g\big(f_1\big(K_1^T X(t)\big) + f_2\big(K_2^T X(t)\big) + f_3\big(K_3^T X(t)\big)\big).$$

Here, $X(t)$, the stimulus input at time t, is projected onto filters K_i, $1 \le i \le 3$. Each filter is a 16-dimensional vector of weights assigned to each component of X; each f_i is a nonlinearity that maps the corresponding projected stimulus into a firing rate. The function $g(x) = e^x$ is the inverse link function for a Poisson GLM. The functions $f_i(x_i(t))$, $1 \le i \le 3$, each a nonlinear function of a single scalar $x_i(t) = K_i^T X(t)$, were parametrized as the linear combination of five cylindrical basis functions (25):

$$f_i(x_i) = \sum_{j=1}^{5} \alpha_{ij}\, \phi_j(x_i), \text{ with } \phi_j(x_i) = \exp\left\{-\frac{\left(x_i - \mu_{ij}\right)}{2\,\sigma^2}\right\}.$$

These cylindrical basis functions allow for nonlinear relationships between mechanical stimulus features and firing rates. The coefficients $\{\alpha_{ij}\}$, $1 \le i \le 3$, $1 \le j \le 5$ that control the linear combinations of cylindrical basis functions as well as the additional model parameters $\{K_i\}$, $1 \le i \le 3$ that specify the neural filters were fit to minimize the negative log likelihood of the observed spike train given the observed stimulus. Spike history terms were omitted from the model for the following reason: since Vg neurons are silent without stimulation and since our stimulus was applied intermittently and had strong autocorrelation, the best predictor of neural firing was the presence of a spike in recent preceding time. This led to large positive weights on the spike history term, which overwhelmed all stimulus-driven response in many neurons. All models were 10-fold cross-validated; 90% of the data were used for parameter fitting, and the resulting model was used to predict $\hat{r}$ for the remaining 10% of the data. This was repeated 10 times, so that every 1-ms bin for which $\hat{r}$ is predicted was at some point not part of the training data used to specify the parameters of the predictive model. Subsequent analyses of the filter weights $\{K_i\}$, $1 \le i \le 3$ for each neuron were performed on mean values obtained by averaging across the 10 cross-validation instances.

For the dropout analysis to establish the relevance of the various input components, we fitted the corresponding predictive models as described above after removing some classes of input components. We found no evidence of overfitting because of too large a parameter space; for instance, the model with the fewest number of parameters (the rotation only model, with only four input components) performed as well as the full model, while other reduced models showed poorer performance than the full model. Models for the 2D whisker description were constructed in the same manner but based on an eight-dimensional input space that included $\{M, F_x, F_y, \Delta\theta\}$ and their temporal derivatives.

We also investigated an alternative approach to modeling the input–output relation of individual neurons, the "spike-triggered mixture model" (26), based on similar input spaces and employing similar parameters. The results were both qualitatively and quantitatively similar; details about these models and their corresponding results are available on request.

Data Availability. Data will be made available upon request. Analyses were performed in MATLAB and Python using custom modules and scripts. This software is available upon request.

ACKNOWLEDGMENTS. This work was supported by NIH Grants R01-NS093585 to M.J.Z.H. and S.A.S., and F31-NS092335 to N.E.B. We thank Admir Resulaj for technical assistance.

1. M. C. Stüttgen, S. Kullmann, C. Schwarz, Responses of rat trigeminal ganglion neurons to longitudinal whisker stimulation. *J. Neurophysiol.* **100**, 1879–1884 (2008).
2. L. M. Jones, D. A. Depireux, D. J. Simons, A. Keller, Robust temporal coding in the trigeminal system. *Science* **304**, 1986–1989 (2004).
3. M. Shoykhet, D. Doherty, D. J. Simons, Coding of deflection velocity and amplitude by whisker primary afferent neurons: Implications for higher level processing. *Somatosens. Mot. Res.* **17**, 171–180 (2000).
4. M. Szwed *et al.*, Responses of trigeminal ganglion neurons to the radial distance of contact during active vibrissal touch. *J. Neurophysiol.* **95**, 791–802 (2006).
5. E. Lottem, R. Azouz, A unifying framework underlying mechanotransduction in the somatosensory system. *J. Neurosci.* **31**, 8520–8532 (2011).
6. R. Storchi, M. R. Bale, G. E. Biella, R. S. Petersen, Comparison of latency and rate coding for the direction of whisker deflection in the subcortical somatosensory pathway. *J. Neurophysiol.* **108**, 1810–1821 (2012).
7. M. R. Bale, K. Davies, O. J. Freeman, R. A. A. Ince, R. S. Petersen, Low-dimensional sensory feature representation by trigeminal primary afferents. *J. Neurosci.* **33**, 12003–12012 (2013).
8. H. Zeng, J. R. Sanes, Neuronal cell-type classification: Challenges, opportunities and the path forward. *Nat. Rev. Neurosci.* **18**, 530–546 (2017).
9. E. E. Kwegyir-Afful, S. Marella, D. J. Simons, Response properties of mouse trigeminal ganglion neurons. *Somatosens. Mot. Res.* **25**, 209–221 (2008).
10. S. H. Lichtenstein, G. E. Carvell, D. J. Simons, Responses of rat trigeminal ganglion neurons to movements of vibrissae in different directions. *Somatosens. Mot. Res.* **7**, 47–65 (1990).
11. M. C. Stüttgen, J. Rüter, C. Schwarz, Two psychophysical channels of whisker deflection in rats align with two neuronal classes of primary afferents. *J. Neurosci.* **26**, 7933–7941 (2006).
12. E. Zucker, W. I. Welker, Coding of somatic sensory input by vibrissae neurons in the rat's trigeminal ganglion. *Brain Res.* **12**, 138–156 (1969).
13. T. A. Woolsey, H. Van der Loos, The structural organization of layer IV in the somatosensory region (SI) of mouse cerebral cortex. The description of a cortical field composed of discrete cytoarchitectonic units. *Brain Res.* **17**, 205–242 (1970).
14. P. M. Knutsen, A. Biess, E. Ahissar, Vibrissal kinematics in 3D: Tight coupling of azimuth, elevation, and torsion across different whisking modes. *Neuron* **59**, 35–42 (2008).
15. D. Deutsch, M. Pietr, P. M. Knutsen, E. Ahissar, E. Schneidman, Fast feedback in active sensing: Touch-induced changes to whisker-object interaction. *PLoS One* **7**, e44272 (2012).
16. S. C. Leiser, K. A. Moxon, Responses of trigeminal ganglion neurons during natural whisking behaviors in the awake rat. *Neuron* **53**, 117–133 (2007).
17. V. Khatri, R. Bermejo, J. C. Brumberg, A. Keller, H. P. Zeigler, Whisking in air: Encoding of kinematics by trigeminal ganglion neurons in awake rats. *J. Neurophysiol.* **101**, 1836–1846 (2009).
18. D. Campagner, M. H. Evans, M. R. Bale, A. Erskine, R. S. Petersen, Prediction of primary somatosensory neuron activity during active tactile exploration. *eLife* **5**, 18 (2016).
19. K. S. Severson *et al.*, Active touch and self-motion encoding by Merkel cell-associated afferents. *Neuron* **94**, 666–676.e9 (2017).
20. E. J. Chichilnisky, A simple white noise analysis of neuronal light responses. *Network* **12**, 199–213 (2001).
21. C. Kayser, R. F. Salazar, P. Konig, Responses to natural scenes in cat V1. *J. Neurophysiol.* **90**, 1910–1920 (2003).
22. G. E. Carvell, D. J. Simons, Biometric analyses of vibrissal tactile discrimination in the rat. *J. Neurosci.* **10**, 2638–2648 (1990).
23. J. A. Hobbs, R. B. Towal, M. J. Z. Hartmann, Spatiotemporal patterns of contact across the rat vibrissal array during exploratory behavior. *Front. Behav. Neurosci.* **9**, 356 (2016).
24. L. A. Huet, C. L. Schroeder, M. J. Z. Hartmann, Tactile signals transmitted by the vibrissa during active whisking behavior. *J. Neurophysiol.* **113**, 3511–3518 (2015).
25. R. S. Williamson, M. Sahani, J. W. Pillow, The equivalence of information-theoretic and likelihood-based methods for neural dimensionality reduction. *PLOS Comput. Biol.* **11**, e1004141 (2015).
26. L. Theis, A. M. Chagas, D. Arnstein, C. Schwarz, M. Bethge, Beyond GLMs: A generative mixture modeling approach to neural system identification. *PLOS Comput. Biol.* **9**, e1003356 (2013).
27. E. Ahissar, P. M. Knutsen, Object localization with whiskers. *Biol. Cybern.* **98**, 449–458 (2008).
28. M. Szwed, K. Bagdasarian, E. Ahissar, Encoding of vibrissal active touch. *Neuron* **40**, 621–630 (2003).
29. N. E. Bush *et al.*, Decoupling kinematics and mechanics reveals coding properties of trigeminal ganglion neurons in the rat vibrissal system. *eLife* **5**, e13969 (2016).
30. N. G. Clack *et al.*, Automated tracking of whiskers in videos of head fixed rodents. *PLOS Comput. Biol.* **8**, e1002591 (2012).
31. J. M. Gibson, W. I. Welker, Quantitative studies of stimulus coding in first-order vibrissa afferents of rats. 1. Receptive field properties and threshold distributions. *Somatosens. Res.* **1**, 51–67 (1983).
32. J. M. Gibson, W. I. Welker, Quantitative studies of stimulus coding in first-order vibrissa afferents of rats. 2. Adaptation and coding of stimulus parameters. *Somatosens. Res.* **1**, 95–117 (1983).
33. L. M. Jones, S. Lee, J. C. Trageser, D. J. Simons, A. Keller, Precise temporal responses in whisker trigeminal neurons. *J. Neurophysiol.* **92**, 665–668 (2004).

34. M. Mazurek, M. Kager, S. D. Van Hooser, Robust quantification of orientation selectivity and direction selectivity. *Front. Neural Circuits* **8**, 92 (2014).
35. S. A. Hires, D. A. Gutnisky, J. Yu, D. H. O'Connor, K. Svoboda, Low-noise encoding of active touch by layer 4 in the somatosensory cortex. *eLife* **4**, e06619 (2015).
36. N. E. Bush, S. A. Solla, M. J. Z. Hartmann, Whisking mechanics and active sensing. *Curr. Opin. Neurobiol.* **40**, 178–188 (2016).
37. A. Bjorck, G. H. Golub, Numerical methods for computing angles between linear subspaces. *Math. Comput.* **27**, 579–594 (1973).
38. P. Gao, S. Ganguli, On simplicity and complexity in the brave new world of large-scale neuroscience. *Curr. Opin. Neurobiol.* **32**, 148–155 (2015).
39. L. A. Huet, M. J. Z. Hartmann, Simulations of a vibrissa slipping along a straight edge and an analysis of frictional effects during whisking. *IEEE Trans. Haptics* **9**, 158–169 (2016).
40. P. M. Knutsen, E. Ahissar, Orthogonal coding of object location. *Trends Neurosci.* **32**, 101–109 (2009).
41. S. Tonomura *et al*., Structure-function correlations of rat trigeminal primary neurons: Emphasis on club-like endings, a vibrissal mechanoreceptor. *Proc. Jpn. Acad., Ser. B, Phys. Biol. Sci.* **91**, 560–576 (2015).
42. E. Lottem, E. Gugig, R. Azouz, Parallel coding schemes of whisker velocity in the rat's somatosensory system. *J. Neurophysiol.* **113**, 1784–1799 (2015).
43. S. J. Whiteley, P. M. Knutsen, D. W. Matthews, D. Kleinfeld, Deflection of a vibrissa leads to a gradient of strain across mechanoreceptors in a mystacial follicle. *J. Neurophysiol.* **114**, 138–145 (2015).
44. B. T. Fundin, K. Pfaller, F. L. Rice, Different distributions of the sensory and autonomic innervation among the microvasculature of the rat mystacial pad. *J. Comp. Neurol.* **389**, 545–568 (1997).
45. Y. Luo, C. S. Bresee, J. W. Rudnicki, M. J. Z. Hartmann, Constraints on the deformation of the vibrissa within the follicle. *PLOS Comput. Biol.* **17**, e1007887 (2021).
46. L. L. Li, D. D. Ginty, The structure and organization of lanceolate mechanosensory complexes at mouse hair follicles. *eLife* **3**, e01901 (2014).
47. S. Maksimovic *et al*., Epidermal Merkel cells are mechanosensory cells that tune mammalian touch receptors. *Nature* **509**, 617–621 (2014).
48. M. Nakatani, S. Maksimovic, Y. Baba, E. A. Lumpkin, Mechanotransduction in epidermal Merkel cells. *Pflugers Arch.* **467**, 101–108 (2015).
49. S. Ebara, K. Kumamoto, T. Matsuura, J. E. Mazurkiewicz, F. L. Rice, Similarities and differences in the innervation of mystacial vibrissal follicle-sinus complexes in the rat and cat: A confocal microscopic study. *J. Comp. Neurol.* **449**, 103–119 (2002).
50. H. Hayashi, Distributions of vibrissae afferent fiber collaterals in the trigeminal nuclei as revealed by intra-axonal injection of horseradish peroxidase. *Brain Res.* **183**, 442–446 (1980).
51. M. F. Jacquin, W. E. Renehan, R. D. Mooney, R. W. Rhoades, Structure-function relationships in rat medullary and cervical dorsal horns. I. Trigeminal primary afferents. *J. Neurophysiol.* **55**, 1153–1186 (1986).
52. D. J. Field, What is the goal of sensory coding? *Neural Comput.* **6**, 559–601 (1994).
53. S. P. Jadhav, D. E. Feldman, Texture coding in the whisker system. *Curr. Opin. Neurobiol.* **20**, 313–318 (2010).
54. A. Wallach, K. Bagdasarian, E. Ahissar, On-going computation of whisking phase by mechanoreceptors. *Nat. Neurosci.* **19**, 487–493 (2016).
55. Y. S. W. Yu, M. M. Graff, C. S. Bresee, Y. B. Man, M. J. Z. Hartmann, Whiskers aid anemotaxis in rats. *Sci. Adv.* **2**, e1600716 (2016).
56. F. L. Rice, A. Mance, B. L. Munger, A comparative light microscopic analysis of the sensory innervation of the mystacial pad. I. Innervation of vibrissal follicle-sinus complexes. *J. Comp. Neurol.* **252**, 154–174 (1986).
57. C. Rossant *et al*., Spike sorting for large, dense electrode arrays. *Nat. Neurosci.* **19**, 634–641 (2016).
58. L. A. Huet, J. W. Rudnicki, M. J. Z. Hartmann, Tactile sensing with whiskers of various shapes: Determining the three-dimensional location of object contact based on mechanical signals at the whisker base. *Soft Robot.* **4**, 88–102 (2017).
59. B. W. Quist, M. J. Z. Hartmann, Mechanical signals at the base of a rat vibrissa: The effect of intrinsic vibrissa curvature and implications for tactile exploration. *J. Neurophysiol.* **107**, 2298–2312 (2012).
60. B. W. Quist, V. Seghete, L. A. Huet, T. D. Murphey, M. J. Z. Hartmann, Modeling forces and moments at the base of a rat vibrissa during noncontact whisking and whisking against an object. *J. Neurosci.* **34**, 9828–9844 (2014).
61. J. W. Pillow *et al*., Spatio-temporal correlations and visual signalling in a complete neuronal population. *Nature* **454**, 995–999 (2008).